Characterization of Transitional, High-Enthalpy Boundary Layers on a Slightly-Blunted Cone. Part II: FLDI and Higher-Order Spectral Analysis

A. Hameed[*] and N. J. Parziale[†]
Stevens Institute of Technology, Hoboken, NJ 07030, USA.

L. Paquin,[‡]
U.S. Naval Research Laboratory, Washington, DC 20375, USA

S. J. Laurence[§]
University of Maryland, College Park, MD 20742, USA

W. M. Yu[¶] and J. M. Austin[‖]
California Institute of Technology, Pasadena, CA 91125, USA

FLDI is used to characterize an unstable boundary layer on a 5° cone. Results from two experiments are presented: shot 2990 represented a high-enthalpy condition with a 2 mm nosetip and shot 2955 represented a moderate-enthalpy condition with a 5 mm nosetip. For shot 2990, the measured frequency of the second-mode instability using FLDI agreed well with the results obtained using schlieren for an experiment performed at similar conditions, and was in good agreement with the maximum N factor frequency obtained using stability analysis. Cross-bicoherence analysis of the FLDI data revealed several sum and difference interactions which contributed to the generation of the first and second harmonics of the second mode within the boundary layer as well as provided the mechanism of energy exchange between the second mode and the mean flow.

I. Introduction

The transition of a hypervelocity boundary layer to turbulence can increase surface heating loads by a factor of 4-10 [1]. However, there is considerable uncertainty associated with the location of boundary-layer transition in the hypersonic flow regime, which limits the optimization of hypersonic vehicle design. To protect the vehicle from overheating, designers of hypersonic vehicles accommodate for this unpredictability using thermal protection systems with large factors of safety. A better estimate of the boundary-layer transition location is required to optimize the thermal protection system and improve vehicle performance, payload capacity, and reduce vehicle cost [2].

Boundary-layer transition in hypersonic flow at zero angle of attack is affected by receptivity to freestream disturbances leading to the growth of dominant eigenmodes known as Mack's first and second modes [2]. The viscous first-mode instability is stabilized with increasing Mach number, whereas the inviscid, acoustic in nature, second-mode instability is amplified as its growth rate exceeds that of the first-mode with increasing Mach number [3]. It becomes the dominant instability wave in the hypersonic regime for Mach numbers greater than 4 for insulated surfaces and lower Mach numbers for cooled surfaces [4]. The second-mode instability belongs to the family of trapped acoustic waves, with the boundary layer behaving as an acoustic waveguide [4], propagating with a phase speed approximately equal to the boundary-layer edge velocity with dominant frequencies ranging from 100 kHz to over 1 MHz [5]. Since its theoretical conception, the second mode has been experimentally observed using various flow measurement techniques. Demetriades [6] performed experiments at $M_\infty = 8$ over a very sharp 5° half-angle cone, where he photographed

---

*Graduate Student, Mechanical Engineering, 1 Castle Point on Hudson, Hoboken, New Jersey, 07030, USA.
†Associate Professor, Mechanical Engineering, 1 Castle Point on Hudson, Hoboken, New Jersey, 07030, AIAA Associate Fellow.
‡Aerospace Engineer, Naval Center for Space Technology, U.S. Naval Research Laboratory, Washington, DC 20375, AIAA Member.
§Associate Professor, Aerospace Engineering, Department of Aerospace Engineering, College Park, Maryland, 20742. Senior AIAA Member.
¶PhD Candidate, Graduate Aerospace Laboratories, 1200 E. California Blvd, MC 105-50.
‖Professor of Aerospace, Graduate Aerospace Laboratories, 1200 E. California Blvd, MC 105-50, Associate Fellow AIAA.

the rope-like nature of the second-mode instability using shadowgraphs. He concluded the waves were concentrated near the boundary-layer edge and were "made up of density crests and valleys as opposed to velocity fluctuations." Kendall [7] performed constant-current hot-wire anemometry experiments at $M_\infty = 8.5$ over a sharp, $4°$ half-angle cone and measured signatures of large amplitude, periodic waves at $3.43 \times 10^6\,m^{-1} \le Re \le 8.60 \times 10^6\,m^{-1}$, which he identified with the second-mode instability. In another set of experiments, Demetriades [8] estimated the frequency of the second-mode instability to be proportional to the boundary-layer edge velocity and inversely proportional to the boundary-layer thickness ($f = U_e/2\delta$). More recently, Laurence [9] applied image processing techniques to high-speed schlieren sequences to obtain structural and propagation characteristics of the second-mode instability waves. Parziale et al. [10, 11] demonstrated the ability to measure the second-mode instability in a reflected-shock tunnel by using focused laser differential interferometry (FLDI) on a slender body at Caltech's T5.

Although the second-mode instability has been extensively studied by researchers, the nonlinear interactions between the second-mode instability and other disturbances is not well understood. Using hot-wire anemometry data from experiments performed on a sharp cone at $M_\infty = 7.95$ by Stetson, et al. [12] in AEDC Tunnel B, Kimmel and Kendall [13] found evidence of nonlinear wave propagation not accounted for by linear theory. They used bicoherence methods to show phase coherence between the second-mode instability and its first harmonic, suggesting the low frequency disturbances modulate frequencies near the second mode and its first harmonic. Shiplyuk [14] observed the subharmonic resonance of the second mode was the dominant nonlinear interaction. Chokani [15] studied the evolution of nonlinear disturbances in a transitioning hypersonic boundary layer. He characterized the transition process as a series of discrete sum and difference nonlinear interactions between the Mack mode, the mean flow, or the first harmonic. By determining the cross-bicoherence of hot-wire data, he found that nonlinear disturbances evolved due to a phase-locked difference interaction that involved energy exchange between the Mack mode and the mean flow and were immediately followed by a sum interaction of the Mack mode to generate the first harmonic. He also quantified the destabilizing effect of wall cooling on the transitioning boundary layer by observing nonlinear interactions between the Mack mode and its harmonic to occur further upstream on a cooled wall than on an adiabatic wall.

Developed by Smeets[16–21] and Smeets and George[22] in the 1970s, the focused laser differential interferometer is a common path, polarizing interferometer sensitive to the phase difference between the interfering beam pairs. It is used to measure density variations in gas flows, featuring excellent spatial and temporal resolution (<100 μm and 10 MHz), as well as high sensitivity at low densities (0.1 g/m^3)[23]. Smeets and George used FLDI to measure the density profile within a shock front, unsteady boundary layers, and, amongst other things, developed an eight beam pair FLDI set-up to examine the flow field around a blunt cone. Following the work of Smeets and George, researchers used laser differential interferometry (LDI) to make measurements in high speed flows[24–29]. In 2012, Parziale et al.[10, 11, 30–34] advanced the FLDI technique and used it to characterize the facility disturbance level and boundary-layer instability and transition in the Caltech T5 reflected-shock tunnel. Researchers have recently used the technique to make reliable measurements of convective velocity between two closely spaced FLDI probe volumes[23, 35–41], facility disturbance-level characterization[42–44], and have developed beam shaping techniques for application of the technique in hard-to-access flows.[45–49]. Researchers have used controlled problems[50–52] to test the data-reduction strategies developed by Fulghum[53], Settles and Fulghum[54], Schmidt and Shepherd[55], and Hameed and Parziale[56].

In this work, we use a multi-beam FLDI setup to probe the flow over a blunted cone at various wall-normal positions. We use higher order spectral analysis to determine the degree of coherence between the measurements taken within and outside of the boundary layer. Experiments during this campaign were also performed using high-speed schlieren, and those results are presented in part I [57].

II. Facility and Experimental Setup

A. T5 Reflected-Shock Tunnel

The experiments in this campaign were performed at California Institute of Technology's T5 free-piston-driven reflected-shock tunnel. By generating high enthalpy flows at high density, this facility simulates the chemical nonequilibrium effects of vehicles flying at hypervelocity speeds through the atmosphere. Additional information regarding the capabilities of T5 can be found in Hornung [58].

In T5, a 120 kg aluminum piston is loaded into the compression tube/secondary reservoir junction. A 127 μm thick Mylar secondary diaphragm is inserted at the nozzle throat, separating the shock tube from the test section prior to the experiment. A 7-10 mm thick stainless steel primary diaphragm is inserted between the compression tube and the shock

tube. Once the facility reaches an acceptable level of vacuum, the shock tube is filled with the test gas (ALPHAGAZ air for these experiments), the compression tube is filled with a He/Air mixture, and the secondary reservoir is pressurized with air. The air in the secondary reservoir is then allowed to push against the back of the piston and the piston is launched into the compression tube. The accelerating piston adiabatically compresses the driver gas in the compression tube until the primary diaphragm ruptures. The rupture of the primary diaphragm causes a shock wave to propagate into the shock tube, which reflects off the end wall, bursts the secondary diaphragm, and re-processes the test gas to the nozzle reservoir conditions. The test gas is then expanded through the converging-diverging contoured nozzle to a hypersonic Mach number ($M \approx 5.2$) in the test section.

We use the nozzle reservoir conditions to estimate the freestream run conditions. The thermodynamic state of the test gas in the nozzle reservoir is determined using the shock tube pressure, P_1, and the measured incident shock speed, U_s. Using Cantera[59] with the Shock and Detonation Toolbox[60], we assume isentropic expansion of this state to the reservoir pressure, P_R, accounting for weak expansion or compression waves that are reflected between the contact surface and the shock tube end wall. The calculated nozzle reservoir conditions are inputted into the University of Minnesota Nozzle Code to determine the freestream conditions at the exit of the contoured nozzle [61–64]. The reservoir and freestream run conditions for the shots performed in this experimental campaign are presented in Table 1 and Table 2. The freestream conditions are chosen to be an areal average of the DPLR output at approximately 420±10 mm, the distance from the throat to the location of the nose tip.

A slightly-blunted 5° half-angle cone was used as the model in this experimental campaign. Two cone nose-tip bluntnesses (R_N) were used in this experimental campaign and the cone was placed at zero angle of attack in the center of the test section.

Table 1   Reservoir Conditions

| Shot	Gas	P_R	h_R	T_R	ρ_R	y_{N_2}	y_{O_2}	y_{NO}	y_N	y_O	R_N	Diag
		(MPa)	(MJ/kg)	(K)	(kg/m^3)	(-)	(-)	(-)	(-)	(-)	(mm)	(-)
2983	Air	53.5	9.48	5962	28.3	0.700	0.054	0.135	0.004	0.107	2	Schlieren
2984	Air	55.8	9.60	6021	29.2	0.699	0.053	0.136	0.005	0.108	2	Schlieren
2985	Air	58.1	9.03	5794	32.0	0.699	0.064	0.140	0.003	0.095	2	Schlieren
2986	Air	59.9	8.98	5780	33.1	0.699	0.065	0.140	0.003	0.093	2	Schlieren
2987	Air	58.9	8.85	5724	33.0	0.699	0.067	0.141	0.003	0.091	2	Schlieren
2988	Air	60.1	8.93	5758	33.4	0.699	0.066	0.141	0.003	0.092	2	Schlieren
2989	Air	60.1	9.74	6098	31.0	0.699	0.051	0.136	0.005	0.109	2	Schlieren
2990	Air	59.6	8.86	5727	33.3	0.699	0.068	0.141	0.003	0.090	2	FLDI
2991	Air	57.6	8.80	5695	32.4	0.699	0.068	0.140	0.003	0.090	2	FLDI
2992	Air	59.9	8.44	5552	34.9	0.699	0.077	0.142	0.002	0.081	3	FLDI
2993	Air	60.7	8.07	5396	36.6	0.700	0.086	0.142	0.001	0.072	3	Schlieren

B. FLDI Setup

The components used to generate the FLDI diagnostic employed in this experimental campaign are shown in Fig. 1. A 532 nm, linearly polarized beam output from a Cobolt 05-01 series single frequency, CW diode pumped laser was first expanded using a diverging lens. Two diffractive optics (Holo/Or MS-474-Q-Y-A and DS-192-Q-Y-A) were used to generate a grid of beams. The grid of beams passed through a quarter-wave plate, and then were split once more into orthogonally polarized beam pairs by a 2-arcminute Wollaston prism. The beams passed through a converging lens and entered the test section. The positioning of the diverging lens (C_1 in Fig. 1) was adjusted relative to the upbeam converging lens (C_2 in Fig. 1) to locate the focus of the beams at the top of the cone. The height of the beams was adjusted such that the lowest set of beams were located at approximately one half of the boundary-layer height. Downbeam of the test section, the diverging FLDI beam pairs were again brought to a focus using a converging lens (C_2 in Fig. 1). The four beam pairs were recombined using a Wollaston prism of an equivalent separation angle, linearly polarized, and directed onto individual photodetectors.

For shot 2990, the streamwise beam interspacing was 1.71 mm, the wall-normal beam interspacing was 1.02 mm, and the streamwise beam intraspacing was 0.18 mm. The lower set of beams were positioned at a height of approximately

Table 2   Freestream Conditions

Shot	U_X	ρ_X	P_X	T_X	Tv_X	M_X	Re_X^U	y_{N_2}	y_{O_2}	y_{NO}	y_N	y_O
	(m/s)	(kg/m³)	(kPa)	(K)	(K)	(-)	(1/m)	(-)	(-)	(-)	(-)	(-)
2983	3913	0.075	32.1	1472	1480	5.05	5.33e+06	0.733	0.183	0.073	0.000	0.011
2984	3935	0.078	33.7	1495	1502	5.04	5.48e+06	0.733	0.183	0.073	0.000	0.011
2985	3839	0.084	33.8	1388	1397	5.11	6.07e+06	0.733	0.186	0.073	0.000	0.008
2986	3831	0.087	34.6	1379	1387	5.12	6.29e+06	0.733	0.187	0.073	0.000	0.007
2987	3808	0.086	33.8	1354	1363	5.13	6.28e+06	0.733	0.187	0.073	0.000	0.007
2988	3822	0.087	34.6	1369	1377	5.12	6.35e+06	0.733	0.187	0.073	0.000	0.007
2989	3963	0.083	36.6	1523	1530	5.02	5.80e+06	0.733	0.183	0.073	0.000	0.011
2990	3809	0.087	34.2	1355	1363	5.13	6.35e+06	0.733	0.187	0.073	0.000	0.007
2991	3797	0.084	32.9	1343	1352	5.14	6.18e+06	0.733	0.187	0.073	0.000	0.007
2992	3735	0.089	32.5	1265	1274	5.21	6.63e+06	0.732	0.188	0.074	0.000	0.005
2993	3664	0.092	31.7	1191	1200	5.28	7.04e+06	0.732	0.189	0.076	0.000	0.004
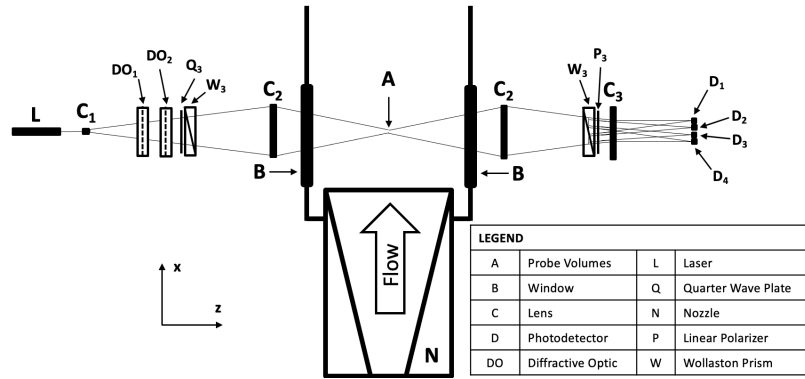
Fig. 1   Optical components used to generate the FLDI diagnostic in this experimental campaign.

0.6 mm above the cone's surface. The streamwise interspaced and intraspaced beams were oriented to be parallel to the cone surface and the wall-normal interspaced beams were oriented to be perpendicular to the cone surface.

A picture of the beams at the focus taken using an Ophir-Spiricon LT-665 beam profiler is shown in Fig. 2. For shot 2990, we interrogated the flow using the column of upstream beam pairs and the lowest row of beam pairs. This selection allowed two beam pairs to be within the boundary layer (FLDI probes C and D) and two beam pairs to be at various heights above the boundary layer (FLDI probes A and B). The boundary layer was determined to be approximately 1.1 mm thick at the measurement location of 680 mm along the cone. The velocity profile at this position is represented in Fig. 2 as a solid white line. Both the boundary-layer thickness and the velocity profile were determined using DPLR.

III. Results and Discussion

In this section, we begin by presenting results for shot 2990, an experiment representing a transitional boundary layer with a 2 mm nose-tip at relatively high enthalpy (8.9 MJ/kg). The experiment conditions of shot 2990 were similar to those of shot 2988, allowing for a comparison between the results obtained using FLDI and schlieren. Fig. 3 shows the reservoir pressure trace for shot 2990, with the red line indicating the average reservoir pressure for the test duration (1.05-2.15 ms).
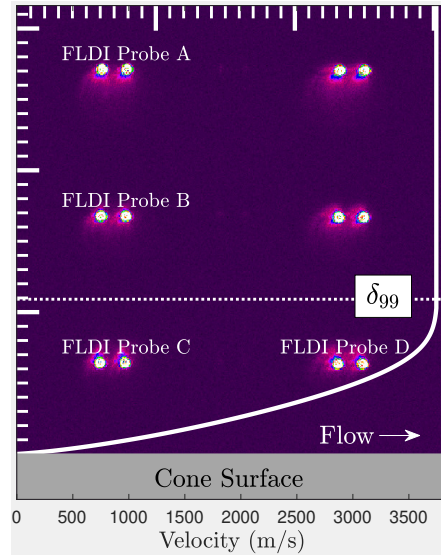
Fig. 2   Picture of the positioning of FLDI beam pairs for shot 2990. The major tick marks are spaced 1 mm apart and the minor tick marks are spaced 0.1 mm apart. The beams are located approximately 0.635 mm above the cone surface. The velocity profile is given by the solid white line and the boundary-layer thickness is depicted by the dotted line. The flow is from left to right.
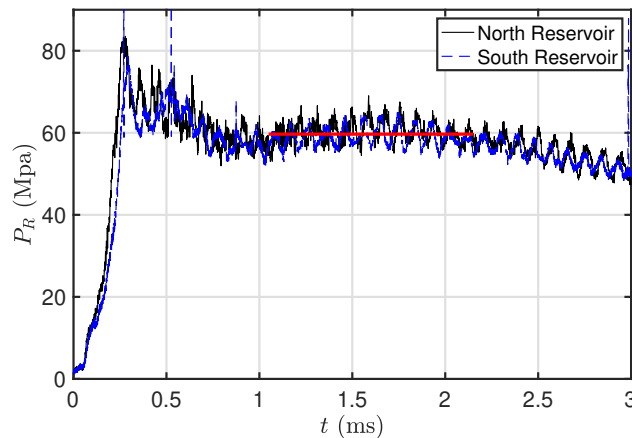

Fig. 3   Reservoir pressure trace for shot 2990. The red line indicates the average reservoir pressure for the test duration.

A. Power Spectral Density

Fig. 4a to Fig. 4d show the spectrograms for the four FLDI probes throughout the test time with the addition of a time delay to account for the time needed to accelerate the flow from the reservoir, through the nozzle, and into the test section. The spectrogram for probes C and D (the two FLDI probes within the boundary layer at approximately 0.6 mm above the cone surface) shows the second-mode instability intermittently present during the test time. The second-mode instability is not seen in the spectrograms for probes A and B (the two probes outside of the boundary layer). Rather, a broadband burst is observed in these spectrograms at discrete instances in time, with many of these bursts corresponding to instances where the second-mode instability was observed in probes C and D. The averaged power spectral density (PSD) for this experiment is shown in Fig. 4e. FLDI probes C and D show distinct peaks representing the second-mode instability at approximately f_{2M} = 1250 kHz. The black line in Fig. 4e represents the maximum N factor curve as estimated from stability calculations for this shot performed with PSE-Chem, which is a part of the STABL software package described in Johnson et al.[63, 65] We note that the maximum N factor of 12.6 occurred at a peak disturbance frequency of 1435 kHz. We suspect this difference in measured second-mode frequency and calculated peak disturbance

5

frequency could be attributed to an error in the calculation of the run condition resulting in an incorrect calculation of the mean flow, or the model having a slight angle of attack relative to the flow.

Next, we take a short-time Fourier transform from 2335 μs to 2380 μs to investigate the burst seen in the spectrograms of probes A and B (Fig. 4a, Fig. 4b) during that time. The resulting spectrograms and the short-time PSD are presented in Fig. 5. The spectrograms for FLDI probes A (Fig. 5a) and B (Fig. 5b) show the broadband nature of the burst, while the spectrograms for FLDI probes C (Fig. 5c) and D (Fig. 5d) show that the second-mode instability is present in this shorter time duration. The short-time PSD also reveals elevated low-frequency content measured by FLDI probes A and B, which had been averaged out during the longer time duration. Higher-frequency disturbances are also observed in the short-time PSDs for probes C and D at the second-mode instability's first harmonic ($2f_{2M} \approx 2600$ kHz).

B. Higher-Order Spectral Analysis

We further investigate the coherence between the bursts observed by probes A and B and the second-mode instability measured by probes C and D using the Higher-Order Spectral Analysis (HOSA) toolbox in MATLAB. Higher-order spectral analysis is used to characterize the nonlinear interactions between the various disturbances in a hypersonic boundary layer. Higher order spectral analysis has been used in the study of hypersonic boundary layers to characterize the evolution of nonlinear disturbances [15], show harmonic generation due to phase coupling between Mack-mode waves [66, 67] and to identify the existence of subharmonic resonance at the initial stage of transition [14].

The cross-bispectrum is defined as,

$$S_{xyz}(f_1, f_2) = \int_{-\infty}^{\infty} \int_{-\infty}^{\infty} R_{xyz}(\tau, \lambda) e^{-i2\pi f_1 \tau} e^{-i2\pi f_2 \lambda} d\tau d\lambda \tag{1}$$

where, $R_{xyz}(\tau, \lambda) = E\{x^*(t)y(t+\tau)z(t+\lambda)\}$ is the cross-correlation. Normalizing the cross-bispectrum provides the cross-bicoherence, and in this work, the cross-bicoherence is estimated using the `bicoherx` function in the HOSA Toolbox in MATLAB. There are various methods of normalizing the bispectrum, and the strategy employed in the HOSA toolbox is similar to the one suggested by Brillinger [68]. The cross-bicoherence is used to characterize the interactions between two spatially separated signals, and is defined as,

$$b_{xyz}(f_1, f_2) = \frac{S(f_1, f_2)}{\sqrt{S(f_1 + f_2)S(f_1)S(f_2)}}, \tag{2}$$

where $S(f)$ is the PSD power. It is estimated by the `bicoherx` function as

$$\text{bic}(f_1, f_2) = \frac{|B(f_1, f_2)|^2}{P(f_1 + f_2)P(f_1)P(f_2)}, \tag{3}$$

where $B(f_1, f_2)$ is the averaged estimate of the cross-bispectrum and $P(f)$ are the averaged estimates of the power spectra. In this work, we take the square-root of the output of the `bicoherx` function to get the cross-bicoherence in the form as defined above.

Disturbances that are independently excited at the frequency triad, f_1, f_2, and $f_1 + f_2$ are statistically independent of each other and show no peaks in the cross-bicoherence spectrum. Peaks in the cross-bicoherence spectrum indicate a quadratic phase coupling (QPC) interaction exists between the frequency triad, f_1, f_2, and $f_1 + f_2$, and the nonlinear interaction $(f_1, f_2) \rightarrow f_1 + f_2$, where the symbol $\rightarrow$ denotes "generated by phase-locked interaction." [15] The identified phase-locked interactions can either be sum or difference interactions. Sum interactions are associated with the frequency triad f_1, f_2, and $f_{sum}(= f_1 + f_2)$, and are present in the cross-bicoherence map within the triangle formed by the symmetry line $f_1 = f_2$, the horizontal axis, and $f_n/2$, where f_n is the Nyquist frequency. Difference interactions are associated with the frequency triad f_1, $-f_2$, and $f_{difference}(= f_1 - f_2)$, and are present in the region of the cross-bicoherence spectrum bounded by the symmetry line $f_1 = -f_2$, the horizontal axis, and $f_n/2$. In this paper, the axes of the cross-bicoherence maps for shot 2990 are normalized by the frequency of the second-mode instability. To facilitate the interpretation of the peaks in the cross-bicoherence, the average of the PSD curves for the two signals being investigated is presented on the left and to the bottom of the cross-bicoherence map. Additionally, the intensity scaling is consistent betweeen all cross-bicoherence maps and limited to show peaks with $b \geq 0.25$ at contour intervals of 0.1.

Fig. 6 shows the cross-bicoherence computed between the spatially separated FLDI probes during the burst seen from 2335 μs to 2380 μs. Fig. 6a provides the cross-bicoherence between probes C and D. Fig. 6b and Fig. 6c provide the cross-bicoherence between probes C and A, B, respectively. Fig. 6d and Fig. 6e provide the cross-bicoherence
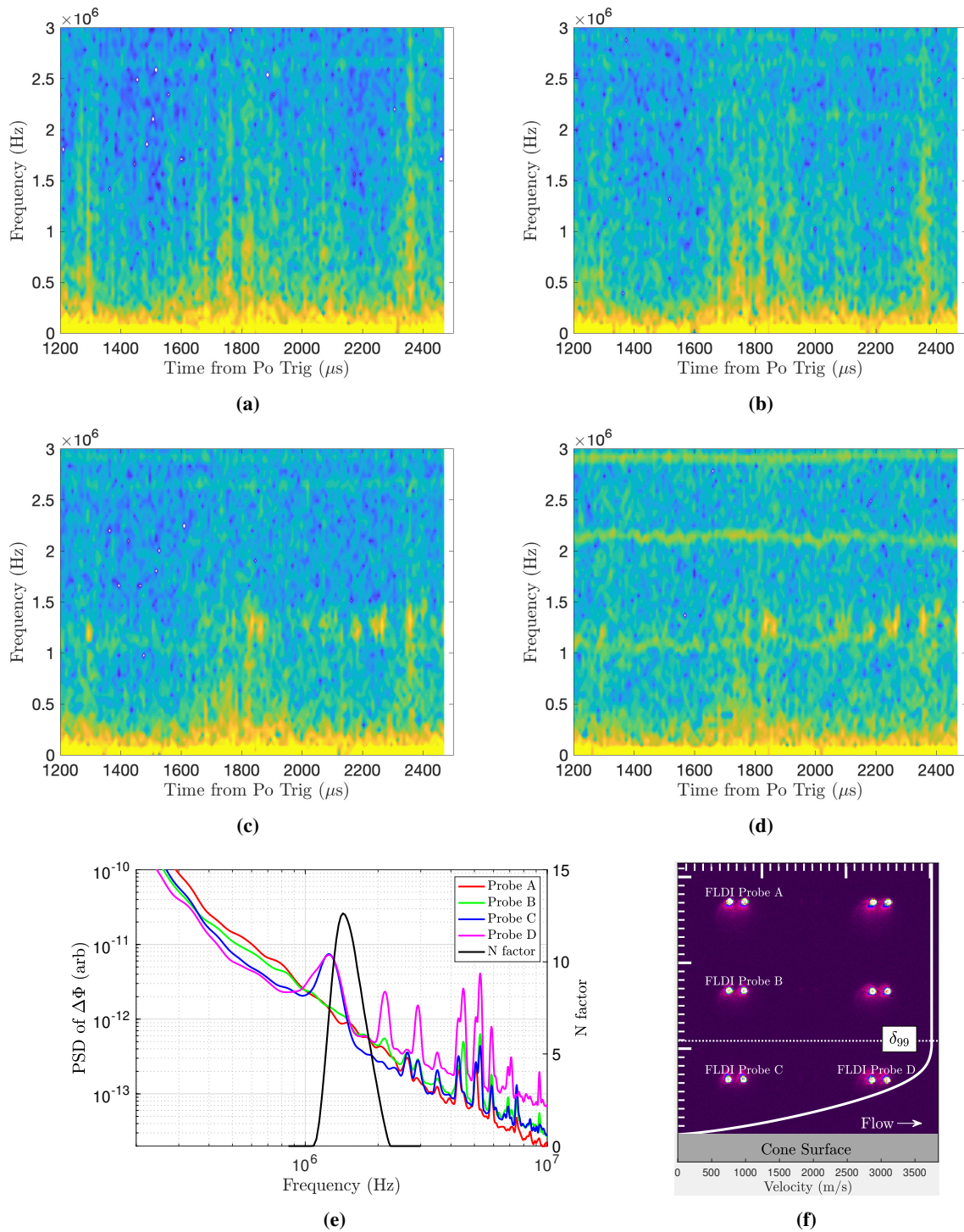
Fig. 4   For shot 2990, (a) to (d) spectrograms for FLDI probes A, B, C, and D, respectively. The spectrograms for probes C and D, which are located inside the boundary layer, show the second-mode instability. This feature is not present in the spectrograms for probes A and B. (e) Average corrected PSD for all four FLDI probes, showing the second-mode instability at approximately 1250 kHz measured by probes C and D in the boundary layer. (f) FLDI probe locations relative to the surface of the cone provided for clarity.
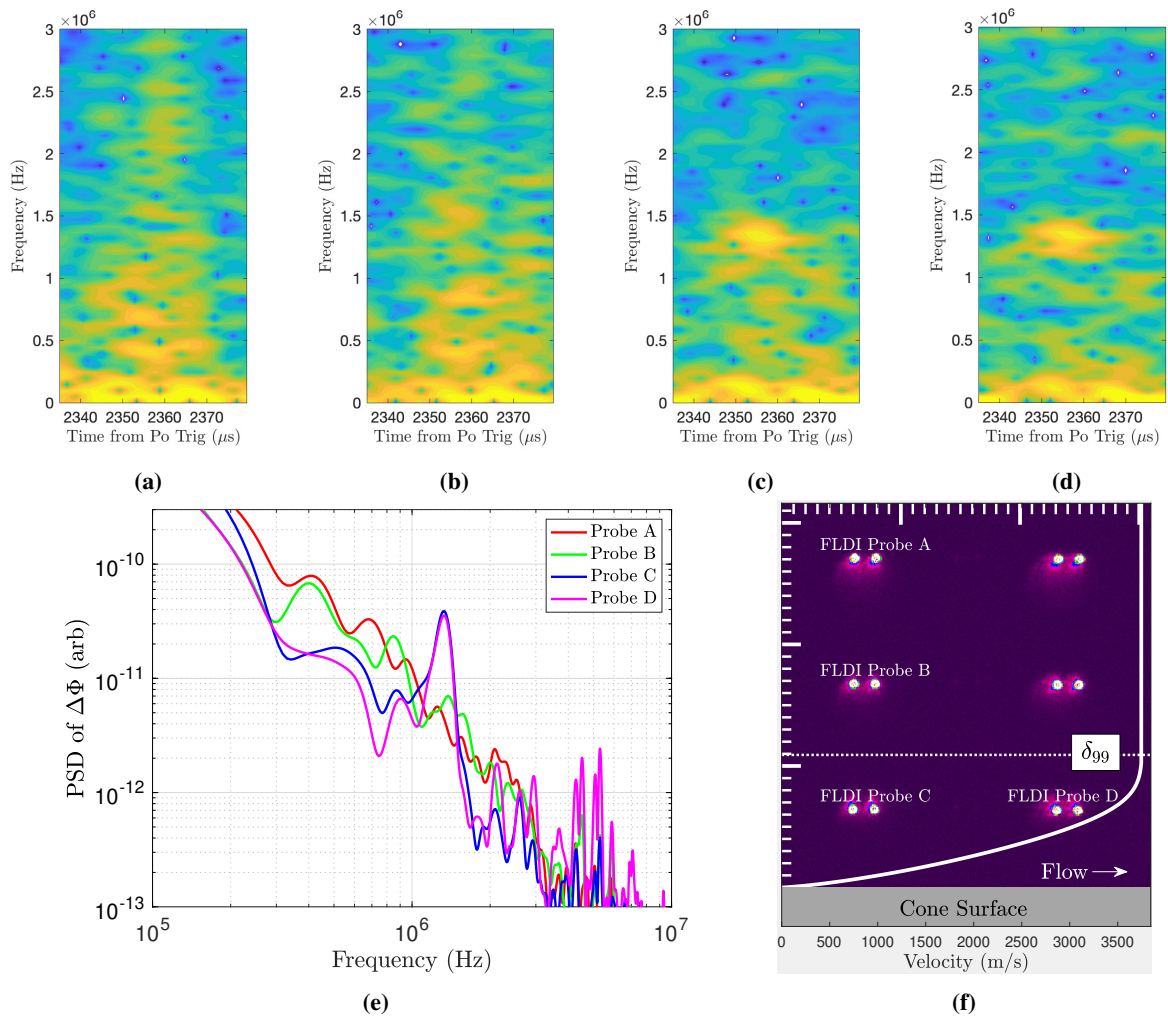
Fig. 5   For shot 2990, (a) to (d) short-time spectrograms for FLDI probes A, B, C, and D, respectively and (e) short-time corrected PSD for all four FLDI probes, showing the second-mode instability and its first harmonic measured by probes C and D. (f) FLDI probe locations relative to the surface of the cone provided for clarity.

8

between probes D and A, B, respectively. The strongest interactions occur between probes C and D, both of which are located within the boundary layer, and are separated along the direction of the flow. The strong sum interaction at $(f_{2M}, f_{2M}) \rightarrow 2f_{2M}$ is the nonlinear mechanism by which the first harmonic of the second mode is generated, and is the likely cause of the peak observed in the short-time PSDs of both probes C and D at approximately 2600 kHz. The sum interaction at $(2f_{2M}, f_{2M}) \rightarrow 3f_{2M}$ identifies the nonlinear mechanism by which the second harmonic of the second mode is generated. The difference interaction at $(2f_{2M}, -f_{2M}) \rightarrow f_{2M}$ provides the nonlinear mechanism through which energy is exchanged between the second mode and its first harmonic within the boundary layer. This difference interaction was also present in the cross-bicoherence analysis of schlieren data from shot 2988, and was identified in Ref. [57] to be the strongest interaction within the boundary layer for that experiment. Additional interactions between the second mode and frequencies 60-80% of the fundamental are also observed between the probes within the boundary layer for shot 2990, consistent with results for shot 2988 obtained using data from high-speed schlieren. Weaker nonlinear interactions exist between probes within the boundary layer and those outside. In Fig. 6b, the range of sum interactions extending from the abscissa to the symmetry line at $0.5f_{2M}$ likely contribute to the generation of the subharmonic peak and elevated low-frequency spectral content observed in the PSD for probe A. Sum and difference interactions between the second-mode and low frequencies are observed in the cross-bicoherence maps of FLDI probes C and B and FLDI probes D and B. These phase-locked interactions broaden the sidebands of the second-mode during the initial stages of nonlinear evolution. Difference interactions of moderate intensity are observed in the cross-bicoherence maps between probes C and A, B (Figs. 6b and 6c) and probes D and B (Fig. 6e) at $(f_{2M}, -f_{2M}) \rightarrow 0$, indicating energy exchange between the second mode and the mean flow. [15]

C. Spectral Analysis of Shot 2955

We next analyze shot 2955. The reservoir and freestream conditions for shot 2955 can be found in Hameed et al. [69]. Shot 2955 was a transitional experiment with moderate enthalpy in which a 5 mm blunt nosetip was used (in comparison to the 2 mm blunt nosetip used for shot 2990). For shots 2990 and 2955, Fig. 7 shows the entropy layer thickness as a dashed line calculated using Eq. 1 in Hameed et al. [69] and the boundary-layer thickness as a solid line. In shot 2990, the entropy layer is swallowed by the boundary layer at approximately 165 mm along the cone, more than 100 boundary-layer thicknesses away from the FLDI measurement location of 680 mm. For shot 2955, the entropy layer remains thicker than the boundary layer at the FLDI measurement location of approximately 650 mm along the cone. The boundary layer finally swallows the entropy layer at 745 mm along the cone.

In shot 2955, the four FLDI probes were arranged in a square orientation, with probes A and C located in the outside of the boundary layer and entropy layer and probes B and D within the entropy layer and boundary layer (Fig. 8f). We focus on a burst seen in the averaged spectrograms of all four probes from 1500 μs to 1600 μs. The short-time spectrograms and spectra for all four probes during this time duration are presented in Fig. 8. We note the elevated low frequency spectral content for the probes outside of the boundary layer and entropy layer as well as the peaks periodically observed at discrete frequencies by all four probes.

To further investigate relationships between the disturbances measured by the four spatially separated probes, we perform higher order spectral analysis for the signals from shot 2955. The cross-bicoherence maps are presented in Fig. 9. In these maps, the axes are not normalized by the second-mode frequency as one could not be ascertained from the spectra. In general, the cross-bicoherence maps show a higher degree of phase locking between the two probes outside of the boundary layer and entropy layer (probes A and C, Fig. 9a), suggesting the elevated spectral content measured in this region could be due to nonlinear phase-locked interactions. The most intense of these interactions are primarily sum interactions at frequencies corresponding to peaks observed in the spectra. There is also a notable gap in phase-locked interactions observed in all of the cross-bicoherence maps below approximately 500 kHz. Further analysis of experimental results and computational work is necessary to provide context to these features.

IV. Conclusions

In this paper, FLDI was used to characterize the transitional boundary layer on a 5° cone. Results from two experiments are presented: shot 2990 represented a high-enthalpy condition with a 2 mm nosetip and shot 2955 represented a moderate-enthalpy condition with a 5 mm nosetip. For shot 2990, the second-mode instability was measured within the boundary layer at a frequency of approximately 1250 kHz, agreeing well with the results obtained using schlieren for an experiment performed at similar conditions, and in good agreement with the maximum N factor frequency obtained using stability analysis. A short time PSD and spectrograms centered around a broadband burst seen in the probes outside of the boundary layer revealed elevated spectral content at low frequencies. Higher order spectral
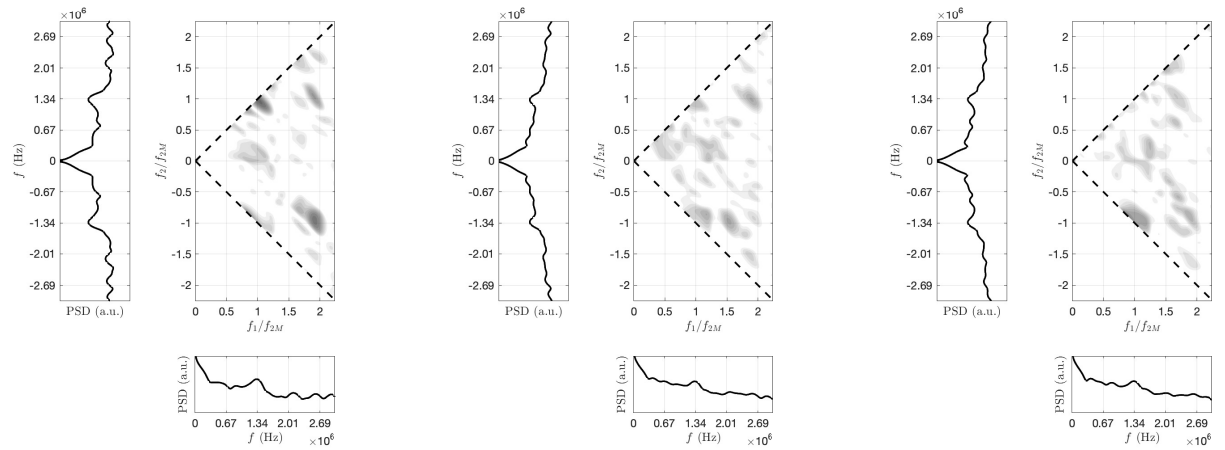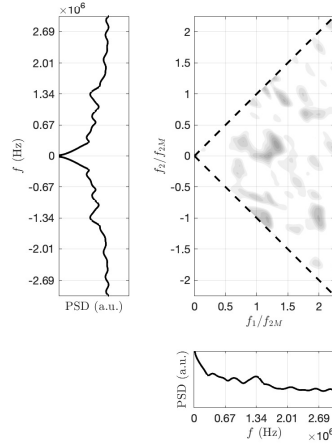
(a) Cross-bicoherence, probes C and D
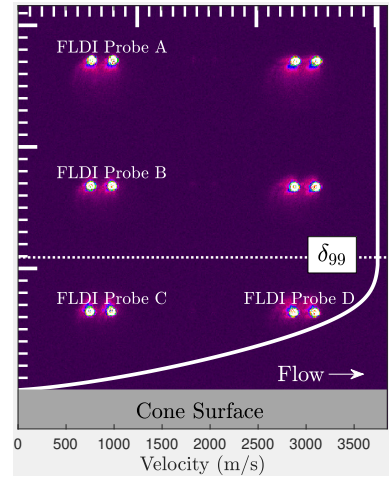

(b) Cross-bicoherence, probes C and A

(c) Cross-bicoherence, probes C and B
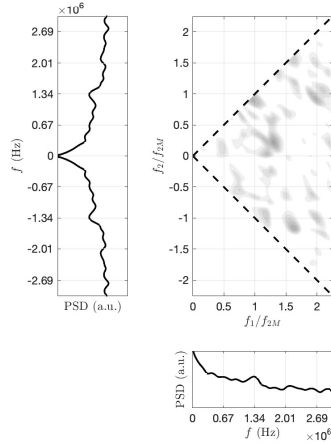
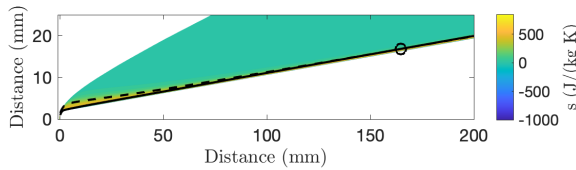**(d) Cross-bicoherence, probes D and A**
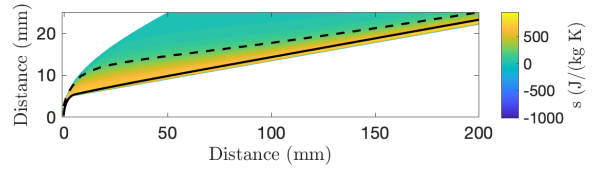

(e) Cross-bicoherence, probes D and B

(f)

Fig. 6 Cross-bicoherence maps for Shot 2990. In these figures, and in subsequent cross-bicoherence maps, the dashed line represents the line of symmetry $f_1 = \pm f_2$. (f) FLDI probe locations relative to the surface of the cone provided for clarity.

(a)

(b)

Fig. 7 Entropy layer swallowing lengths for (a) shot 2990 and (b) shot 2955. The entropy layer thickness is denoted by the dashed line and the boundary-layer thickness is depicted by the solid line. In shot 2990, the entropy layer is swallowed by the growing boundary layer at 165 mm along the cone (marked by the circle), whereas in shot 2955 the swallowing length is 745 mm along the cone (not visible in the figure).
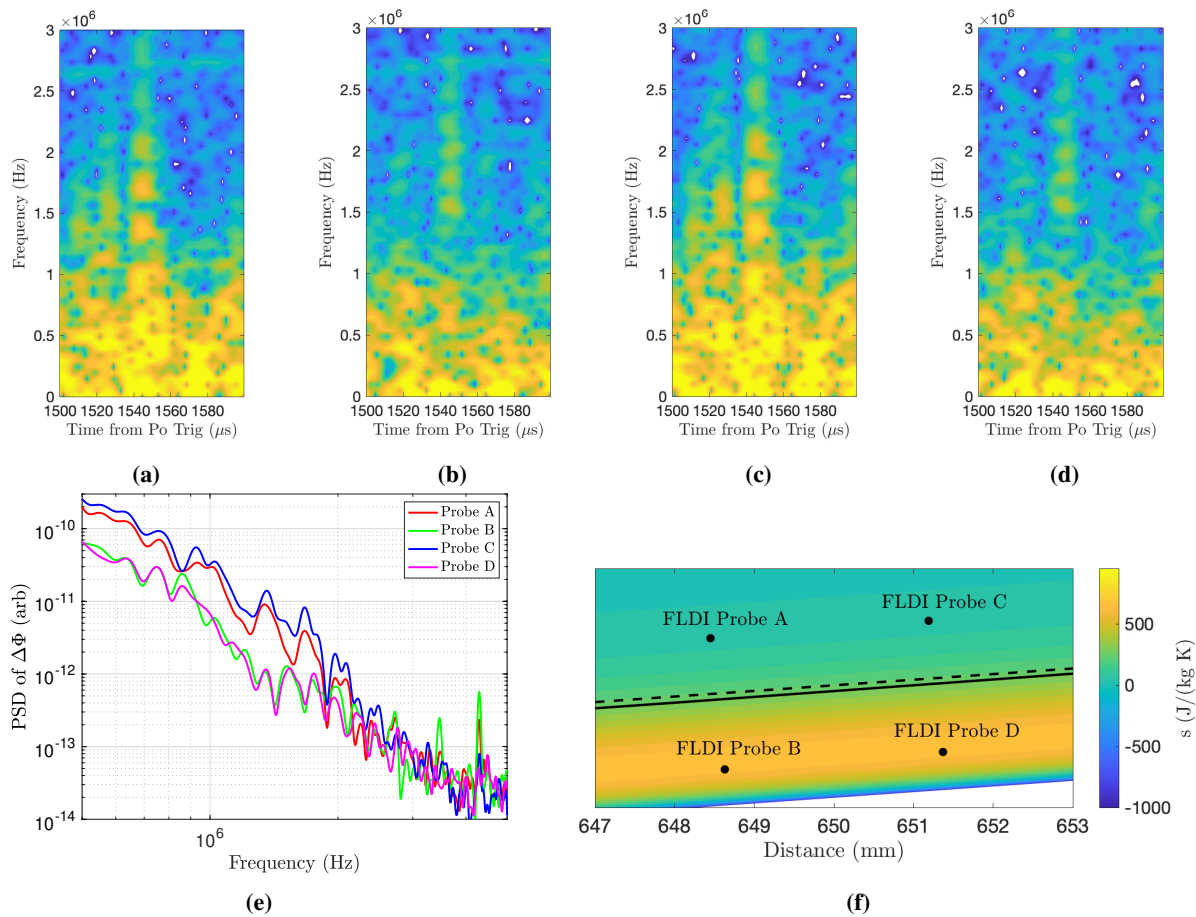
10

Fig. 8   For shot 2955, (a) to (d) short-time spectrograms for FLDI probes A, B, C, and D, respectively and (e) short-time corrected PSD for all four FLDI probes. (f) A depiction of the wall-normal positions of the FLDI probes at the measurement location of 650 mm.
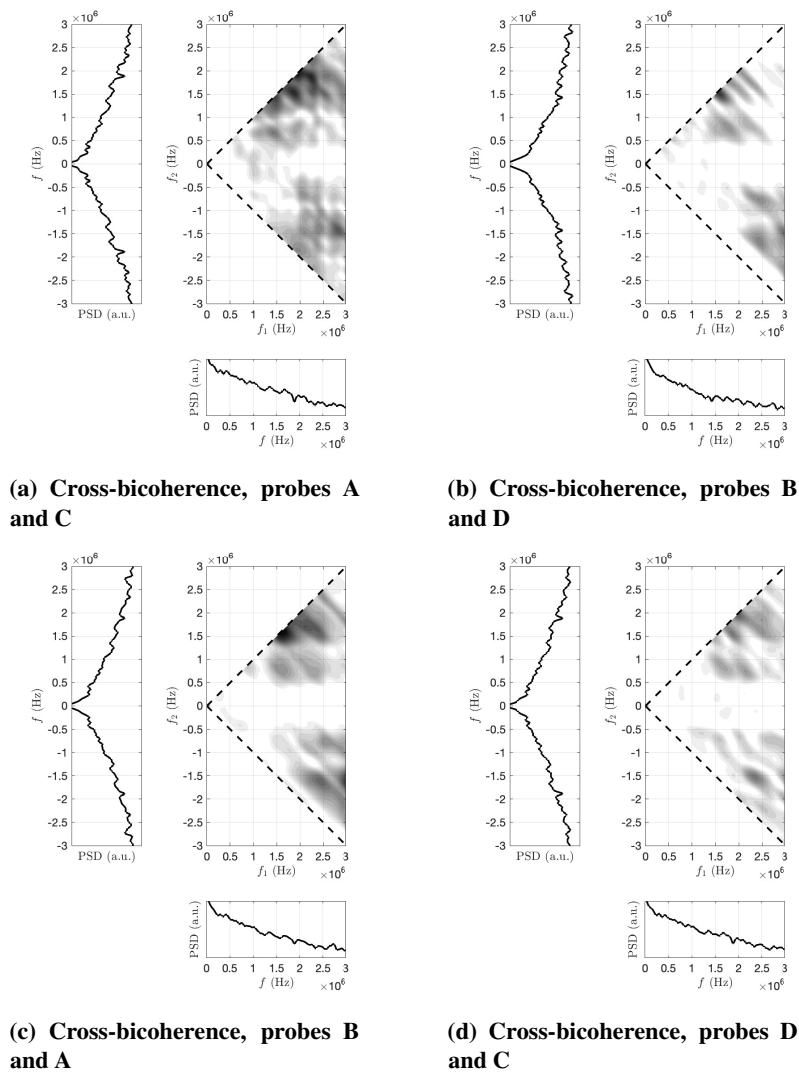
(a) Cross-bicoherence, probes A and C

(b) Cross-bicoherence, probes B and D

(c) Cross-bicoherence, probes B and A

(d) Cross-bicoherence, probes D and C

Fig. 9   Cross-bicoherence maps for Shot 2955.

analysis, namely cross-bicoherence analysis, was used to determine the degree of coherence between the spatially separated FLDI signals. The cross-bicoherence analysis revealed several sum and difference interactions between the probes within the boundary layer contributing to the generation of the first and second harmonics of the second mode and providing the nonlinear mechanism for energy exchange between the second-mode and its first harmonic. These nonlinear interactions identified within the boundary layer using FLDI data supported cross-bicoherence results obtained using schlieren data. Weaker sum and difference interactions were observed between FLDI probes inside and outside of the boundary layer. These sum interactions contributed to the elevated low frequency spectral content observed outside of the boundary layer and the difference interactions suggested the exchange of energy between the second mode and the mean flow.

A few interesting features were observed in the spectrogram and spectra for shot 2955. The two FLDI probes positioned outside the boundary layer and entropy layer exhibited higher spectral content than those inside the boundary layer/entropy layer. Additionally, the spectra for all four FLDI probes showed periodic peaks observed at discrete frequencies. Cross-bicoherence analysis of FLDI data for this experiment showed strong sum interactions in the outside the boundary layer and entropy layer and a notable gap in phase-locked interactions for all four probes below approximately 500 kHz. Additional analysis is necessary to provide context to these results.

Acknowledgments

References

[1] Bitter, N. P., and Shepherd, J. E., "Stability of highly cooled hypervelocity boundary layers," *Journal of Fluid Mechanics*, Vol. 778, No. 10, 2015, pp. 586–620. https://doi.org/10.1017/jfm.2015.358.

[2] Knisely, C. P., and Zhong, X., "Sound radiation by supersonic unstable modes in hypersonic blunt cone boundary layers. II. Direct numerical simulation," *Physics of Fluids*, Vol. 31, No. 2, 2019, p. 024104. https://doi.org/10.1063/1.5077007.

[3] Mack, L. M., "Boundary-Layer Linear Stability Theory," *AGARD Report 709*, 1984.

[4] Fedorov, A., "Transition and Stability of High-Speed Boundary Layers," *Annual Review of Fluid Mechanics*, Vol. 43, 2011, pp. 79–95. https://doi.org/10.1146/annurev-fluid-122109-160750.

[5] Laurence, S. J., Wagner, A., and Hannemann, K., "Experimental study of second-mode instability growth and breakdown in a hypersonic boundary layer using high-speed schlieren visualization," *Journal of Fluid Mechanics*, Vol. 797, 2016, pp. 471–503. https://doi.org/10.1017/jfm.2016.280.

[6] Demetriades, A., "Hypersonic Viscous Flow Over a Slender Cone. III - Laminar Instability and Transition," *Proceedings of the 7th AIAA Fluid and Plasma Dynamics Conference*, AIAA, Palo Alto, California, 1974. https://doi.org/10.2514/6.1974-535.

[7] Kendall, J. M., "Wind-Tunnel Experiments Relating to Supersonic and Hypersonic Boundary-Layer Transition," *AIAA Journal*, Vol. 13, No. 3, 1975, pp. 290–299. https://doi.org/10.2514/3.49694.

[8] Demetriades, A., "Laminar Boundary Layer Stability Measurements at Mach 7 Including Wall Temperature Effects," AFOSR-TR-77-1311, 1977.

[9] Laurence, S. J., Wagner, A., Hannemann, K., Wartemann, V., Lüdeke, H., Tanno, H., and Itoh, K., "Time-Resolved Visualization of Instability Waves in a Hypersonic Boundary Layer," *AIAA Journal*, Vol. 50, No. 6, 2012, pp. 243–246. https://doi.org/10.2514/1.56987.

[10] Parziale, N. J., Shepherd, J. E., and Hornung, H. G., "Observations of hypervelocity boundary-layer instability," *Journal of Fluid Mechanics*, Vol. 781, 2015, pp. 87–112. https://doi.org/10.1017/jfm.2015.489.

[11] Parziale, N. J., "Slender-Body Hypervelocity Boundary-Layer Instability," Ph.D. thesis, California Institute of Technology, 2013.

[12] Stetson, K. F., Thompson, E. R., Donaldson, J. C., and Siler, L. G., "Laminar Boundary Layer Stability Experiments on a Cone at Mach 8, Part 1: Sharp Cone," *Proceedings of the AlAA 16th Fluid and Plasma Dynamics Conference*, AIAA-83-1761, Danvers, Massachusetts, 1983. https://doi.org/10.2514/6.1983-1761.

[13] Kimmel, R., and Kendall, J., "Nonlinear disturbances in a hypersonic laminar boundary layer," *29th Aerospace Sciences Meeting*, 1991, p. 320.

[14] Shiplyuk, A. N., Bountin, D. A., Maslov, A. A., and Chokani, N., "Nonlinear Mechanisms of the Initial Stage of the Laminar-Turbulent Transition at Hypersonic Velocities," *Journal of Applied Mechanics and Technical Physics*, Vol. 44, No. 5, 2003, pp. 654–659. https://doi.org/10.1023/a:1025500219183.

[15] Chokani, N., Bountin, D. A., Shiplyuk, A. N., and Maslov, A. A., "Nonlinear Aspects of Hypersonic Boundary-Layer Stability on a Porous Surface," *AIAA Journal*, Vol. 43, No. 1, 2005, pp. 149–155. https://doi.org/10.2514/1.9547.

[16] Smeets, G., and George, A., "Gas Dynamic Investigations in a Shock Tube using a Highly Sensitive Interferometer," Translation of ISL Internal Report 14/71, Original 1971, Translation 1996.

[17] Smeets, G., "Laser Interferometer for High Sensitivity Measurements on Transient Phase Objects," *IEEE Transactions on Aerospace and Electronic Systems*, Vol. AES-8, No. 2, 1972, pp. 186–190. https://doi.org/10.1109/TAES.1972.309488.

[18] Smeets, G., and George, A., "Anwendungen des Laser-Differentialinterferometers in der Gasdynamik," ISL - N 28/73, Also translated by Goetz, A.: ADA-307459, 1973.

[19] Smeets, G., "Laser-Interferometer mit grossen, fokussierten Lichtbündeln für lokale Messungen," ISL - N 11/73, 1973.

[20] Smeets, G., "Verwendung eines Laser-Differentialinterferometers zur Bestimmung lokaler Schwankungsgrössen sowie des mittleren Dichteprofils in cinem turbulenten Freistrahl," ISL - N 20/74, 1974.

[21] Smeets, G., "Flow Diagnostics by Laser Interferometry," *IEEE Transactions on Aerospace and Electronic Systems*, Vol. AES-13, No. 2, 1977, pp. 82–90. https://doi.org/10.1109/TAES.1977.308441.

[22] Smeets, G., and George, A., "Laser Differential Interferometer Applications in Gas Dynamics," Translation of ISL Internal Report 28/73, Original 1975, Translation 1996.

[23] Ceruzzi, A. P., and Cadou, C. P., "Simultaneous Velocity and Density Gradient Measurements using Two-Point Focused Laser Differential Interferometry," *Proceedings of AIAA Scitech 2019*, AIAA-2019-2295, San Diego, California, 2019. https://doi.org/10.2514/6.2019-2295.

[24] Azzazy, M., Modarress, D., and Hoeft, T., "High Sensitivity Boundary Layer Transition Detector," *Proceedings of SPIE Vol. 569 High Speed Photography, Videography, and Photonics I/I*, SPIE, San Diego, CA, 1985. https://doi.org/10.1117/12.949865.

[25] Azzazy, M., Modarress, D., and Trolinger, J. D., "Feasibility Study of Optical Boundary Layer Transition Detection Method," NASA-CR-178109, 1986.

[26] Azzazy, M., Modarress, D., and Hoeft, T., "High-sensitivity density fluctuation detector," *Journal of Physics E: Scientific Instruments*, Vol. 20, No. 4, 1987, p. 428. https://doi.org/10.1088/0022-3735/20/4/017.

[27] O'Hare, J. E., "A Nonperturbing Boundary-Layer Transition Detector," *Proceedings of SPIE 0569, High Speed Photography, Videography, and Photonics III*, San Diego, California, 1985, pp. 58–63. https://doi.org/10.1117/12.949864.

[28] Collicott, S. H., Schneider, S. P., and Messersmith, N. L., "Review Of Optical Diagnostic Methods For Hypersonic Low-Noise Facilities," *Proceedings of 34th Aerospace Sciences Meeting and Exhibit*, AIAA-96-0851, Reno, NV, 1996. https://doi.org/10.2514/6.1996-851.

[29] Salyer, T. R., Collicott, S. H., and Schneider, S. P., "Feedback Stabilized Laser Differential Interferometry for Supersonic Blunt Body Receptivity Experiments," *Proceedings of 38th Aerospace Sciences Meeting and Exhibit*, AIAA-2000-0416, Reno, Nevada, 2000. https://doi.org/10.2514/6.2000-416.

[30] Parziale, N. J., Shepherd, J. E., and Hornung, H. G., "Reflected Shock Tunnel Noise Measurement by Focused Differential Interferometry," *Proceedings of 42nd AIAA Fluid Dynamics Conference and Exhibit*, AIAA-2012-3261, New Orleans, Louisiana, 2012. https://doi.org/10.2514/6.2012-3261.

[31] Parziale, N. J., Jewell, J. S., Shepherd, J. E., and Hornung, H. G., "Optical Detection of Transitional Phenomena on Slender Bodies in Hypervelocity Flow," *Proceedings of RTO Specialists Meeting AVT-200/RSM-030 on Hypersonic Laminar-Turbulent Transition*, NATO, San Diego, California, 2012.

[32] Parziale, N. J., Shepherd, J. E., and Hornung, H. G., "Differential Interferometric Measurement of Instability at Two Points in a Hypervelocity Boundary Layer," *Proceedings of 51st AIAA Aerospace Sciences Meeting Including the New Horizons Forum and Aerospace Exposition*, AIAA-2013-0521, Grapevine, Texas, 2013. https://doi.org/10.2514/6.2013-521.

[33] Parziale, N. J., Shepherd, J. E., and Hornung, H. G., "Differential Interferometric Measurement of Instability in a Hypervelocity Boundary Layer," *AIAA Journal*, Vol. 51, No. 3, 2013, pp. 750–753. https://doi.org/10.2514/1.J052013.

[34] Parziale, N. J., Shepherd, J. E., and Hornung, H. G., "Free-stream density perturbations in a reflected-shock tunnel," *Experiments in Fluids*, Vol. 55, No. 2, 2014, p. 1665. https://doi.org/10.1007/s00348-014-1665-0.

[35] Jewell, J. S., Parziale, N. J., Lam, K.-L., Hagen, B. J., and Kimmel, R. L., "Disturbance and Phase Speed Measurements for Shock Tubes and Hypersonic Boundary-Layer Instability," *Proceedings of 32nd AIAA Aerodynamic Measurement Technology and Ground Testing Conference*, AIAA-2016-3112, Washington, D. C., 2016. https://doi.org/10.2514/6.2016-3112.

[36] Jewell, J. S., Hameed, A., Parziale, N. J., and Gogineni, S. P., "Disturbance Speed Measurements in a Circular Jet via Double Focused Laser Differential Interferometry," *Proceedings of AIAA Scitech 2019*, AIAA-2019-2293, San Diego, California, 2019. https://doi.org/10.2514/6.2019-2293.

[37] Ceruzzi, A. P., Callis, B., Weber, D., and Cadou, C. P., "Application of Focused Laser Differential Interferometry (FLDI) in a Supersonic Boundary Layer," *Proceedings of AIAA Scitech 2020*, AIAA-2020-1973, Orlando, Florida, 2020. https://doi.org/10.2514/6.2020-1973.

[38] Weisberger, J. M., Bathel, B. F., Herring, G. C., King, R. A., Chou, A., and Jones, S. B., "Two-Point Focused Laser Differential Interferometry Second-Mode Measurements at Mach 6," *Proceedings of AIAA Aviation Forum*, AIAA-2019-2903, Dallas, Texas, 2019. https://doi.org/10.2514/6.2019-2903.

[39] Bathel, B. F., Weisberger, J. M., Herring, G. C., King, R. A., Jones, S. B., Kennedy, R. E., and Laurence, S. J., "Two-point, parallel-beam focused laser differential interferometry with a Nomarski prism," *Applied Optics*, Vol. 59, No. 2, 2020, pp. 244–252. https://doi.org/10.1364/AO.59.000244.

[40] Price, T. J., Gragston, M., Schmisseur, J. D., and Kreth, P. A., "Measurement of supersonic jet screech with focused laser differential interferometry," *Applied Optics*, Vol. 59, No. 28, 2020, pp. 8902–8908. https://doi.org/10.1364/AO.402011.

[41] Hameed, A., Parziale, N. J., Paquin, L., Butler, C., and Laurence, S. J., "Spectral Analysis of a Hypersonic Boundary Layer on a Right, Circular Cone," *Proceedings of AIAA SciTech 2020*, AIAA-2020-0362, Orlando, Florida, 2020, pp. 1–14. https://doi.org/10.2514/6.2020-0362.

[42] Harris, A. J., Kreth, P. A., Combs, C. S., and Schmisseur, J. D., "Laser Differential Interferometry and Schlieren as an Approach to Characterizing Freestream Disturbance Levels," *2018 AIAA Aerospace Sciences Meeting*, AIAA 2018-1100, Kissimmee, Florida, 2018. https://doi.org/10.2514/6.2018-1100.

[43] Lawson, J. M., and Austin, J. M., "Expansion Tube Freestream Disturbance Measurements using a Focused Laser Differential Interferometer," *Proceedings of AIAA Scitech 2020*, AIAA-2020-1064, Orlando, Florida, 2020. https://doi.org/10.2514/6.2020-1064.

[44] Birch, B., Buttsworth, D., and Zander, F., "Measurements of freestream density fluctuations in a hypersonic wind tunnel," *Experiments in Fluids*, Vol. 61, No. 158, 2020, pp. 1–13. https://doi.org/10.1007/s00348-020-02992-w.

[45] Hedlund, B., Houpt, A., Gordeyev, S., and Leonov, S., "Measurement of Flow Perturbation Spectra in Mach 4.5 Corner Separation Zone," *AIAA Journal*, Vol. 56, No. 7, 2018, pp. 2699–2711. https://doi.org/10.2514/1.J056576.

[46] Houpt, A. W., and Leonov, S. B., "Focused Laser Differential Interferometer for Supersonic Boundary Layer Measurements on Flat Plate Geometries," *Proceedings of the 2018 Plasmadynamics and Lasers Conference*, AIAA-2018-3434, Atlanta, Georgia, 2018. https://doi.org/10.2514/6.2018-3434.

[47] Houpt, A. W., and Leonov, S. B., "Focused and Cylindrical-Focused Laser Differential Interferometer Characterization of SBR-50 at Mach 2," *Proceedings of AIAA Aviation 2019*, AIAA-2019-3383, Dallas, Texas, 2019. https://doi.org/10.2514/6.2019-3383.

[48] Benitez, E. K., Jewell, J. S., and Schneider, S. P., "Focused Laser Differential Interferometry for Hypersonic Flow Instability Measurements with Contoured Tunnel Windows," *Proceedings of AIAA Scitech 2020*, AIAA-2020-1282, Orlando, Florida, 2020. https://doi.org/10.2514/6.2020-1282.

[49] Benitez, E. K., Esquieu, S., Jewell, J. S., and Schneider, S. P., "Instability Measurements on an Axisymmetric Separation Bubble at Mach 6," *Proceedings of AIAA Aviation 2020*, AIAA-2020-3072, Virtual Event, 2020. https://doi.org/10.2514/6.2020-3072.

[50] Ramprakash, A., McIntyre, T. J., Wheatley, V., and Mee, D. J., "Performance Analysis of FLDI Technique using Turbulent Jets," *Proceedings of the IX Australian Conference on Laser Diagnostics*, Adelaide, Australia, 2019.

[51] Lawson, J. M., Neet, M. C., Grossman, I. J., and Austin, J. M., "Characterization of a Focused Laser Differential Interferometer," *Proceedings of AIAA Scitech 2019*, AIAA-2019-2296, San Diego, California, 2019. https://doi.org/10.2514/6.2019-2296.

[52] Lawson, J. M., Neet, M. C., Grossman, I. J., and Austin, J. M., "Static and dynamic characterization of a focused laser differential interferometer," *Experiments in Fluids*, Vol. 61, No. 187, 2020, pp. 1–11. https://doi.org/10.1007/s00348-020-03013-6.

[53] Fulghum, M. R., "Turbulence measurements in high-speed wind tunnels using focusing laser differential interferometry," Ph.D. thesis, The Pennsylvania State University, 2014.

[54] Settles, G. S., and Fulghum, M. R., "The Focusing Laser Differential Interferometer, an Instrument for Localized Turbulence Measurements in Refractive Flows," *Journal of Fluids Engineering*, Vol. 138, No. 10, 2016, p. 101402. https://doi.org/10.1115/1.4033960.

[55] Schmidt, B. E., and Shepherd, J. E., "Analysis of focused laser differential interferometry," *Applied Optics*, Vol. 54, No. 28, 2015, pp. 8459–8472. https://doi.org/10.1364/AO.54.008459.

[56] Hameed, A., and Parziale, N. J., "Focused Laser Differential Interferometry Transfer Functions for Complex Density Disturbance Fields," *Proceedings of AIAA Aviation Forum 2021*, AIAA-2021-2907, Virtual Event, 2021. https://doi.org/10.2514/6.2021-2907.

[57] Paquin, L. A., Laurence, S. J., Hameed, A., Parziale, N. J., Yu, W. M., and Austin, J. M., "Characterization of Transitional, High-Enthalpy Boundary Layers on a Slightly-Blunted Cone. Part I: Schlieren Imaging," *Proceedings of AIAA Scitech 2023*, Submitted.

[58] Hornung, H. G., "Performance Data of the New Free-Piston Shock Tunnel at GALCIT," *Proceedings of 17th AIAA Aerospace Ground Testing Conference*, AIAA 1992-3943, Nashville, TN, 1992. https://doi.org/10.2514/6.1992-3943.

[59] Goodwin, D. G., "An Open-Source, Extensible Software Suite for CVD Process Simulation," *Proceedings of CVD XVI and EuroCVD Fourteen, M Allendorf, F Maury, and F Teyssandier (Eds.)*, 2003, pp. 155–162.

[60] Browne, S., Ziegler, J., and Shepherd, J. E., "Numerical Solution Methods for Shock and Detonation Jump Conditions," GALCIT - FM2006-006, Caltech, 2006.

[61] Wright, M. J., Candler, G. V., and Prampolini, M., "Data-parallel Lower-upper Relaxation Method for the Navier-Stokes Equations," *AIAA Journal*, Vol. 34, No. 7, 1996, pp. 1371–1377. https://doi.org/10.2514/3.13242.

[62] Candler, G. V., "Hypersonic Nozzle Analysis Using an Excluded Volume Equation of State," *Proceedings of 38th AIAA Thermophysics Conference*, AIAA-2005-5202, Toronto, Ontario Canada, 2005. https://doi.org/10.2514/6.2005-5202.

[63] Johnson, H. B., "Thermochemical Interactions in Hypersonic Boundary Layer Stabity," Ph.D. thesis, University of Minnesota, Minneapolis , Minnesota, 2000.

[64] Wagnild, R. M., "High Enthalpy Effects on Two Boundary Layer Disturbances in Supersonic and Hypersonic Flow," Ph.D. thesis, University of Minnesota, Minnesota, 2012.

[65] Johnson, H. B., Seipp, T. G., and Candler, G. V., "Numerical Study of Hypersonic Reacting Boundary Layer Transition on Cones," *Physics of Fluids*, Vol. 10, No. 13, 1998, pp. 2676–2685. https://doi.org/10.1063/1.869781.

[66] Chokani, N., "Nonlinear Spectral Dynamics of Hypersonic Laminar Boundary Layer Flow," *Physics of Fluids*, Vol. 11, No. 12, 1999, pp. 3846–3851. https://doi.org/10.1063/1.870243.

[67] Craig, S. A., Humble, R. A., Hofferth, J. W., and Saric, W. S., "Nonlinear behaviour of the Mack mode in a hypersonic boundary layer," *Journal of Fluid Mechanics*, Vol. 872, 2019, pp. 74–99. https://doi.org/10.1017/jfm.2019.359.

[68] Brillinger, D. R., "An introduction to polyspectra," *The Annals of Mathematical Statistics*, 1965, pp. 1351–1374.

[69] Hameed, A., Shekhtman, D., Parziale, N. J., Paquin, L. A., Skinner, S., Laurence, S. J., Yu, W. M., and Austin, J. M., "Hypersonic Boundary-Layer Instability on a Highly Cooled Cone. Part I: Q-FLDI Measurement and Instability Calculations," *Proceedings of AIAA Scitech 2022*, AIAA-2022-0734, San Diego, California and Virtual Event, 2022. https://doi.org/10.2514/6.2022-0734.